Lab on a Chip

PAPER

View Article Online
View Journal | View Issue

Cite this: *Lab Chip*, 2016, **16**, 2302

Metal-insulator-metal waveguides for particle trapping and separation†

Saara A. Khan,*[a] Chia-Ming Chang,[b] Zain Zaidi,[a] Wonseok Shin,[a] Yu Shi,[a] Audrey K. Ellerbee Bowden[a] and Olav Solgaard[a]

Received 17th March 2016,
Accepted 17th May 2016

DOI: 10.1039/c6lc00366d

www.rsc.org/loc

Optical particle trapping and separation are essential techniques in the fields of biology and chemistry. In many applications, it is important to identify passive separation techniques that only rely on intrinsic forces in a system with a fixed device geometry. We present a dual-waveguide sorter that utilizes the loss of metal-insulator-metal (MIM) waveguides for completely passive particle trapping and separation and is created using a unique angle sidewall deposition process. Our experiments show that an inner Au–Si_3N_4–Au waveguide is able to trap particles within the propagation distance of its dominant modes and release the particles into an outer Au–H_2O–Au waveguide. The outer waveguide then propels the particles and separates them by size. The separation results are accurately modeled by a first-principles, analytical model.

Introduction

Laser tweezers[1,2] that can trap and separate particles without fluorescent tags have significant benefits for biological and chemical applications.[3] Laser tweezers are, however, limited by the number of particles they can simultaneously control. In contrast, holographic tweezers and parallel arrays of laser tweezers improve this limitation, but are still limited to small numbers of particles. To meet these challenges, the field of optical trapping[4] has expanded towards using the evanescent fields of waveguides.[5–7]

Waveguides support serial optical traps along the guide and enable control of several particles in parallel. The primary designs for evanescent field-guiding waveguides include slot waveguides,[8,9] bowtie plasmonic tweezers,[10] and channel waveguides.[11–13] Recently, others have shown that waveguides produce sufficient forces to trap, propel, and sort a binary distribution of particle sizes,[14–16] and our group recently demonstrated separation of heterogeneously sized particles in continuous flow.[17] However, many of these methods are active sorting techniques that require the user to manually control the separation process by changing the orientation of light or the device. In this paper we demonstrate passive waveguide sorters with engineered loss that allow separation of heterogeneously sized particles using a fixed device geometry and light orientation; in short, this configuration simplifies position-dependent particle dispensing. These sorters are composed of two metal-insulator-metal (MIM) waveguides fabricated using a double-angled metal deposition technique. The use of double-angled metal deposition *via* electron beams and controlled reactive ion etching leads to more uniform metal sidewall coverage compared to previous RF sputtering techniques.[18] The inner MIM waveguide is used to efficiently trap particles onto the device and propel particles along the guide until the evanescent field decays and the particles are released. Released particles then fall into the force field of the outer MIM waveguide and continue to propagate until the field is attenuated to the point where the propagation force is no longer sufficient. Because less force is required for smaller particles to move, smaller particles propagate further than larger particles, leading to a size-dependent separation. Due to the passive nature of this process, this separation method can be utilized as an effective particle sorting system, which is essential for medical diagnosis, biological applications, and the pharmaceutical industry.[19]

Device structure and principles of operation

Microparticle separation was achieved in a double-core waveguide. The inner waveguide (Fig. 1), composed of Au–Si_3N_4–Au, uses total-internal-reflection as its guiding mechanism, and the gold sidewalls create a very controlled loss in the system. The silicon nitride waveguide "core" is 300 nm tall and 400 nm wide with its gold "cladding" is 50 nm thick. The outer waveguide, composed of Au–H_2O–Au, contains several unguided modes in the SiO_2 substrate, which generate an evanescent field in the Au–H_2O–Au region and also interacts with the gold sidewalls. The gradient of the evanescent field

---

[a] *Department of Electrical Engineering, Stanford University, Stanford, California 94305, USA. E-mail: saarak@stanford.edu*

[b] *Bell Labs, Alcatel-Lucent, 791 Homdel Road, Holmdel, New Jersey 07733, USA*

† Electronic supplementary information (ESI) available. See DOI: 10.1039/c6lc00366d

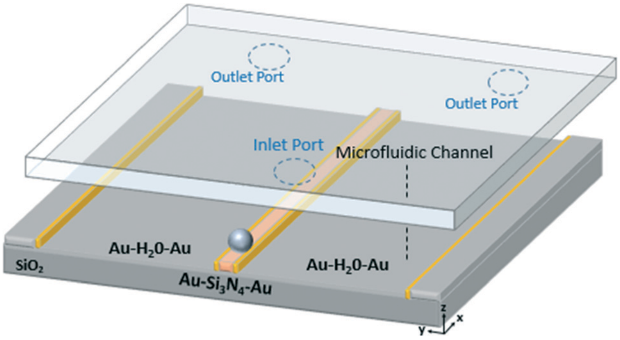

Fig. 1 Schematic of the dual waveguide sorter with an overlaid microfluidic channel.

generated in the water region, in addition to the edges of the gold sidewalls, induce a mechanical force on dielectric particles. We have characterized the fields in COMSOL and used the Maxwell Stress Force Tensor to calculate the optical trapping and propulsion forces particles of various sizes (ESI†). Once the particles have been released from the inner Au–Si_3N_4–Au waveguide, the gradient at the edge of the gold sidewalls attract the particles into the outer water region of the waveguide. The outer waveguide, also shown in Fig. 1, consists of a 10 μm gap filled with water with 50 nm gold sidewalls.

We used silicon dioxide beads to test and verify the sorting capabilities of this structure because they come in a variety of sizes and are straightforward to model in COMSOL due to their spherical shape. A microfluidic chip (PDMS channel of dimensions 100 μm by 100 μm) covered the top of the device to form a channel to contain the silicon dioxide beads in liquid and prevent evaporation. An inlet port was placed at the beginning of the guide, and there were several outlet ports through which the particles could be removed.

To quantify the behaviour of particles in the waveguide trap, we build upon our previous theoretical model[17] to include the losses in the MIM waveguides due to the presence of the gold sidewalls. The forces on a particle suspended in fluid on the waveguide are summarized in the following equation of motion:

$$m\frac{\mathrm{d}^2x}{\mathrm{d}t^2} = F_\mathrm{p} + F_\mathrm{s} + F_\mathrm{D} + F_\mathrm{f}, \tag{1}$$

where m is the mass of the particle, F_p is the optical propulsion force due to the inner and outer guide, F_s is the optical force from the scattered optical fields from the entrance of the waveguides, F_D is the drag force produced by the fluid, and F_f is the mechanical frictional force between the surface of the particle and the waveguide.[20] The drag force on a spherical particle is given by

$$F_\mathrm{D} = -6\pi\eta \mathrm{R}\mathrm{v}(t), \tag{2}$$

where η is the viscosity of the fluid with Faxen's correction,[21] R is the particle radius, and $v(t)$ is the velocity of the particle at time t.

The frictional force is represented by a published model[20] for rolling micron-sized silica particles in water. The model predicts that the rolling adhesion force (h^{ro}) at a distance of 10 nm from the surface will range from 0 to 0.025 nN based on particle size.[20] The 10 nm distance was chosen from expected particle collisions on the surface of the device, which leads to surface force detachment.[22] However, the particle is attracted back to the surface after it is detached because of surface force attraction.[21] The continuous transitions between attractive and repulsive particle movements[23] are estimated to occur 10 nm away from the device surface. The analytical representation of the rolling friction is given by:

$$F_\mathrm{f} = -\mu_\mathrm{ro}\left(\beta mg + F_{g1}\mathrm{e}^{-x(t)/L_\mathrm{p1}} + \alpha\left(F_{g2}\mathrm{e}^{-x(t)/L_\mathrm{p3}}\right) + h^{\mathrm{ro}}\right), \tag{3}$$

$$\begin{aligned} &\alpha = 0,\ \text{if } F_{g1}\mathrm{e}^{-x(t)/L_\mathrm{p1}} > F_\mathrm{thres},\quad \text{and} \\ &\alpha = 1,\ \text{if } F_{g1}\mathrm{e}^{-x(t)/L_\mathrm{p1}} > F_\mathrm{thres}, \end{aligned} \tag{4}$$

where μ_ro is the rolling friction coefficient, β accounts for the buoyancy of the particle in water, g is Earth's gravitational constant, m is the particle's mass, and $x(t)$ is the position of the particle. The mass of the particle is calculated as $m = \rho_\mathrm{glass}\ V = \rho_\mathrm{glass}\left(\frac{4}{3}\right)\pi R^3$, where $\rho_\mathrm{glass} = 2.5\ \mathrm{g\ cm^{-3}}$. The buoyancy factor is computed as $\beta = ((\rho_\mathrm{glass} - \rho_\mathrm{water})/\rho_\mathrm{glass}) = 0.60$. The values for the coefficient of rolling friction are chosen to match the AFM roughness of the silicon nitride surface[20] (see Fig. 7, RMS surface roughness is 5.4 nm) and yield $\mu_\mathrm{ro} = 3.5 \times 10^4$. The optical gradient forces, F_{g1} and F_{g2}, are the forces on the particle pulling it toward the waveguide, which keeps the particle trapped in the evanescent field. We numerically calculated the optical gradient forces for particle sizes 1 , 2 , 3 , and 4 μm in COMSOL (see ESI†). In eqn (4), the variable α is used to represent the transition from the inner to outer guide. The threshold force, F_thres, is defined by the minimum trapping force needed to keep a particle trapped in the evanescent field of a waveguide. We find F_thres by setting α = 0 and determining the value at which $F_\mathrm{f,rolling}$ approximately converges. Using the threshold force, we can use the system of equations to calculate the position at which a particle is released from the inner guide and transitions to the outer guide. Finally, L_p1 and L_p3 are the decay lengths of the inner and outer waveguides.

We define the decay length to be the distance over which the intensity (not the field) decays by a factor of 1/e. We obtained the decay lengths of the inner waveguide by solving the waveguide mode equation[24] for the two lowest-order modes at 1.5 μm using an open-source finite-difference frequency-domain solver[25] (see ESI† for a full sweep of decay lengths of the device between 800 nm and 1.8 μm of the inner waveguide). To visualize the lowest-order modes, we plotted the amplitude of the electric fields (E_x and E_y) using the eigenmode expansion method for mode profiles as shown in

Fig. 2. In our numerical modelling, we assume refractive indices of 2.09 for silicon nitride,[26] 1.5 for silica,[27] 3.44 for silicon,[28] and 0.55 + j9.53 for gold,[29] all at the operating wavelength of 1.5 μm. In addition, optical losses of water at 1.5 μm have been integrated into our initial conditions in COMSOL and FDTD modeling to model optical losses in the region above the waveguide (α = 9.3619 cm^{-1}).[30] The dispersion relation confirms that the fundamental mode, mode 1, has a decay length of L_{p1}=18.9 μm and the second order mode, mode 2, has a decay length of L_{p2} = 14.2 μm. We neglected the second- and higher-order modes because the fundamental mode has the dominant effect in the particle separation in the inner guide.

The outer waveguides contain highly multimodal unguided modes, which induce an optical force on the particles. We have conducted 2-D and 3-D FDTD simulations to analyse this device as shown in the ESI† and found the decay length to be 1.88 mm. Due to the highly multimodal nature of the outer waveguide, we also experimentally obtained the effective decay length of the device and found it to be 1.8 mm (L_{p3}). To separate the measurement of the outer waveguide from the scattering force from the input, we measured the input-to-output loss on devices that were longer than the reach of the scattering force. Based on these propagation lengths, we describe the propulsion force of the system as

$$F_p = F_{p1} e^{-x(t)/L_{p1}} + \alpha\left(F_{p2} e^{-x(t)/L_{p3}}\right), \tag{5}$$

where F_{p1} is the propulsion force from the inner guide, L_{p1} is 18.9 μm, F_{p2} is the propulsion force from the outer guide, L_{p3} is 1.8 mm, and α follows from eqn (4). The optical propulsion forces, F_{p1} and F_{p2}, for 1 , 2 , 3 , and 4 μm particle sizes were calculated numerically in COMSOL (see ESI†).

The scattering force from the input port of the waveguide, F_s, is caused by the unguided light from the excitation of the waveguide. The power of the unguided light falls off as $1/x^2$, which also results in a scattering force that falls off similarly.[31] The scattering force can therefore be described as

$$F_s(x) = \frac{F_{s0}}{(x + x_o)^2}, \tag{6}$$

where x_o is the distance between the beginning of the waveguide to the input laser source, and F_{s0} is used to normalize $F_s(x = 0)$. $F_s(x = 0)$ is found from applying the calculated optical force with the unguided light at the coupling interface of the waveguide. With these descriptions of the forces experienced by the particle, we can numerically evaluate the trajectories of particles with different sizes. Four particles with diameters of 1, 2, 3, and 4 μm were analysed, and Fig. 3 shows the distribution of propulsion forces as a function of position for different particle sizes for the inner and outer guides. As seen in Fig. 3, beyond 100 μm distance, the force on the particles tends to zero and particles must rely on the force from the outer guide to continue traveling. The simulated trajectories of the particles are displayed in Fig. 4. The guided power at the input of the devices is taken at 10 mW for the inner guide, 1 mW for the outer guide, and 200 mW for the scattering light. The values were chosen to approximately match the guided power at the input of the devices in the experimental

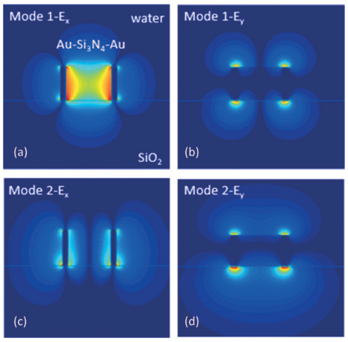

Fig. 2 Mode profiles (amplitude of electric fields) of the Au–SiN–Au waveguide. (a) E$_x$ for the fundamental mode, (b) E$_y$ for the fundamental mode, (c) E$_x$ for the first-order mode, and (d) E$_y$ for the first-order mode.

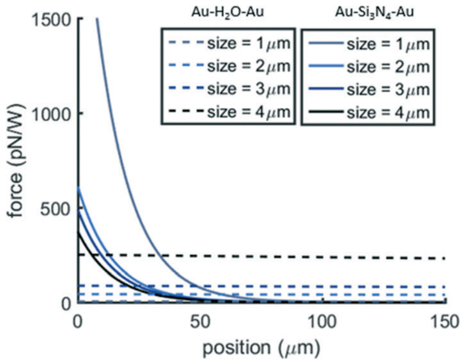

Fig. 3 COMSOL force distribution based on particle size. Forces for the inner waveguide (Au–Si$_3$N$_4$–Au) are displayed with solid lines. Forces for the outer waveguide (Au–H$_2$O–Au) are displayed with dashed lines.

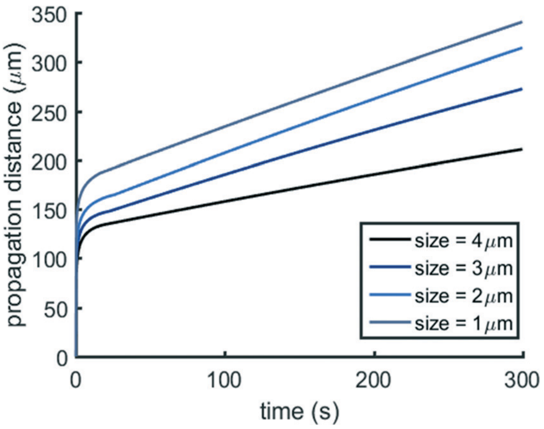

Fig. 4 Simulation data considering force dynamics. Simulation time was limited to 300 seconds based on MATLAB memory space.

section. Based on these distributions we see that particles get momentum from the inner and outer guides to travel a specified distance (based on guided power) and separate by size along the waveguide.

Fabrication and methods

One of the first demonstrations of nanometer-scale sidewall formation was explored and developed for dry-etching-based pattern transfer techniques in 1989 by VanZeghbroeck.[32] In that work, silylation rendered the photoresist much more resistant to oxygen reaction ion etching (RIE) and plasma etching than wet etching. This differential etching responsiveness allowed anisotropic RIE with oxygen to proceed slowly through the silylated layer on top of the structure and continue much more quickly in the unsilylated resist to leave behind free-standing sidewalls after etching. While that technique is still effective in creating free-standing metal sidewalls, it is limited in its ability to create metal sidewalls attached to dielectric structures (such as waveguides). To achieve such sidewalls, recent works have described a method to conduct sidewall transfer lithography using gold nano-sidewalls through a multi-step process using sputtering, anisotropic sputter etching, dry etching by DRIE, and hot embossing.[18] However, these techniques use RF sputtering to coat the silicon mesas with metal, which leads to patchy and non-uniform sidewalls. In this work, we investigated angled electron beam deposition for more uniform metal sidewall coverage on rectangular dielectric waveguides.

We started by fabricating channel waveguides using standard processes and (1) grew a 2 μm oxide layer on a bare silicon wafer using thermal oxidation, (2) deposited 300 nm of high stress nitride on the wafer using low chemical vapour deposition, (3) spun 0.7 μm of photoresist on the wafer, (4) conducted standard photolithography to define 400 nm wide waveguide strips, (5) removed unpatterned nitride using dry plasma etching and (6) removed excess photoresist. The Stanford Crystal Shop then diced and optically polished the wafer into 1 cm by 1 cm devices. This process yielded the structure seen in Fig. 5a.

To achieve waveguides with 50 nm gold sidewalls, we combined metal deposition with significant sidewall coverage and dry etching at normal incidences. For metal depositions, we used an electron beam evaporator in which we attached mounts to the wafer planetary holders to enhance sidewall coverage. We performed deposition at a 14° incident angle relative to normal to achieve 50 nm sidewall coverage on one side of the waveguide (Fig. 6a). To achieve sidewall coverage on the second side, we rotated the wafer by 180° and repeated this process (illustrated in Fig. 5b). We compared the gold coverage using electron beam deposition to RF sputtering methods and found our method gave better uniformity, while RF sputtering led to the gold having patchy sidewalls (see Fig. S3†).

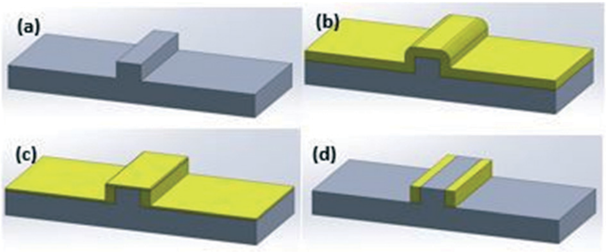

Fig. 5 Schematic of the fabrication procedure involving (a) fabrication of a channel waveguide, (b) deposition of double-angled sidewall metal, (c) etching of the metal, and (d) completion of the etching process to produce metal sidewalls.

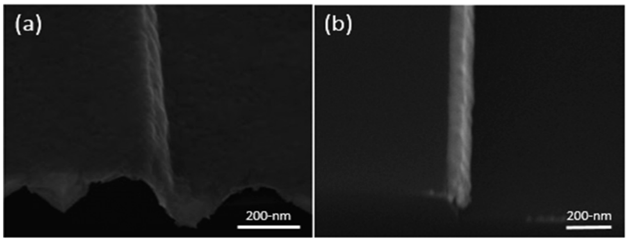

Fig. 6 An SEM image of the device after deposition of double-angled sidewall metal is shown in (a). Gold covers the top of the device and the sidewalls. An SEM image of the device after completing Argon etching is shown in (b) and gold edges are visible.

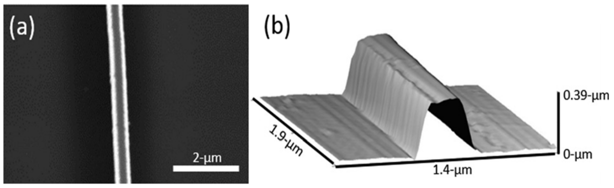

Fig. 7 Images of the final device shown as an SEM image in (a) and in terms of RMS surface roughness in (b).

After the gold deposition, we used a directional Argon plasma RIE system to remove gold on all horizontal surfaces, leaving gold on the vertical sidewalls of the waveguide (Fig. 5c and d). The amount of time needed for directional Argon plasma RIE can depend on the chamber conditioning and plasma settings. Details about RIE characterization of our device and comparison of this technique to RF sputtering can be found in the ESI.† An SEM with one sidewall of the device can be seen in Fig. 6a, and an SEM after Argon plasma RIE can be seen in Fig. 6b. The rectangular cross section of the silicon nitride waveguide causes the gold to conform to the edges of the sidewall. The top view of the waveguide in Fig. 7a clearly shows gold on both sidewalls. The waveguide has a measured surface roughness value of 5.4 nm on the top surface, 3.4 nm on the left sidewall, and 5.4 nm on the right sidewall (Fig. 7b).

The experimental setup consisted of a 1.5 μm semiconductor seed laser amplified in a 30 dB Erbium amplifier connected to a tapered lensed fiber; this created a 2.5 μm spot with 400 mW of TM polarized light for coupling to the inner waveguide at a 14 μm working distance. An identical lensed fiber was coupled to the output of the waveguide to monitor the throughput. The input and output fibers were mounted on piezoelectric XYZ translation stages (ThorLabs MDT693A) to control the coupling. The uncoupled light from the inner waveguide was partly coupled into the two other waveguide channels and partly scattered. We measured the guided power and the coupling loss in the inner waveguide by placing the input fibre at the entrance of the inner waveguide and placing the outer fibre at the output port of the inner waveguide. From this point we optimized the input port until maximum coupling was achieved for the inner waveguide. Keeping the input fibre in its fixed position, we moved the output fibre to one of the outer waveguides to measure the guided power and then scanned the output fibre to the second outer waveguide. If the light has been coupled correctly in the inner waveguide, the guided power in both of the outer waveguides should be similar in guided power within a range of ±1 mW. If the guided power is not similar within this range, the input fibre should be checked again for its coupling. Based on this process, we achieved a coupling and propagation loss for the inner waveguide of 20 dB and 6 dB for the outer waveguides. Scattered light was approximated to be the remaining light that was not measured in the system after all measurements for the guided light were calculated in the inner and outer waveguides.

For an input power of 400 mW, we measured the guided power of the inner guide to be 10 mW, the guided power of the outer guide to be 1 mW, and the scattered light to be approximately 200 mW. The propagation losses in the waveguides accounted for the remainder of the light in the system.

Thermal effects of the 1.5 μm light penetrating into the water are overcome by optimizing coupling into the inner waveguide. This is done by using a tapered fibre tip with a spot diameter of 2.5 ± 0.5 μm and a working distance of 14 ± 2 μm that allows precise coupling into the device compared to a flat-end fibre coupler. In addition, coupling is monitored and maximized at the output port of the inner and outer waveguides. Photothermal effects can be clearly observed when the input fibre is misaligned by 200 nm or more above the waveguide surface, and manifest as the particles experiencing a repelling effect that causes them to move above the device in a convective fluidic flow fashion.[33,34] This characteristic behaviour makes it possible to observe when the device is reacting to the photothermal forces *versus* optical forces and to mitigate photothermal forces.

To test the ability of the waveguide to trap and separate particles of varying sizes, we conducted experiments in which a mixture of silicon dioxide beads (size range 2–10 μm) suspended in distilled water were injected into the inlet port of the microfluidic system. Particle positions were observed with a ThorLabs CMOS camera and an Olympus 20× objective lens.

The camera was used to track particles using a MATLAB program in the following manner: (1) the raw AVI file was converted into a stack of TIFF images, (2) images were converted into grayscale, (3) the image difference was computed, (4) the threshold difference was found, (5) the particles were detected, and (7) the displacement in time for forward moving objects was tracked.

Results

Particles placed at the beginning of the device within 7–10 μm of the inner guide were trapped on the inner guide (images of the trapping process can be found in Fig. S2†). As expected, once particles were trapped, they propagated along the inner guide until the optical power was attenuated to the point where the particles were released, fell into the outer waveguide, and were trapped by it.

Also as expected, release of the particles from the inner guide occurred where the field of the waveguide had decayed to a point where the force from the inner guide is no longer large enough to keep the particles trapped. After this point, the particle fell into the outer guide, as shown in Fig. 8, where it experienced the field generated by this waveguide. The outer waveguide exerted a trapping and propulsion force on the particle. Fig. 9 shows the particle trajectory in the outer waveguide as the particle continues to propagate along the guide. Eventually, the particle came to a stop when the outer field decayed to the point where it can no longer overcome the frictional forces. The particle propagation distance depended on its size (as the force on the particles is size

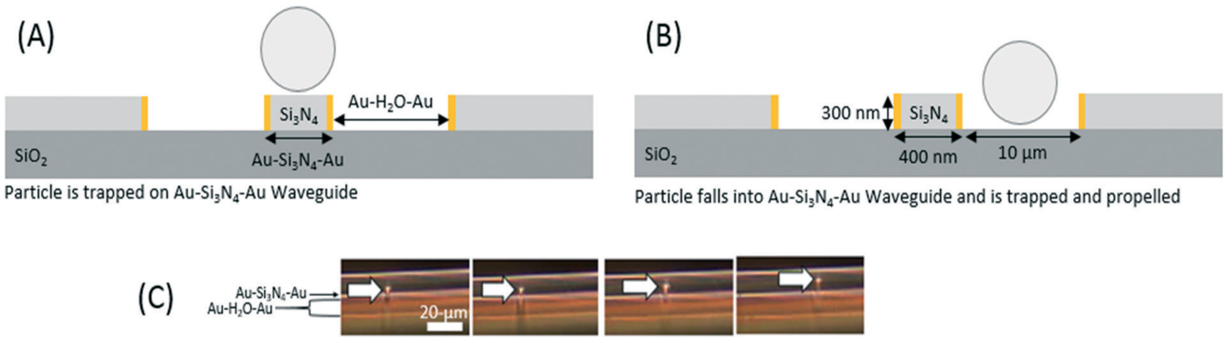

Fig. 8 The particle transition between the inner (A) and outer waveguide (B) is shown in the schematic and microscope images (C). Please note that the schematic is not to scale and the particle sizes used in the experiment are 2–10 μm in size.

Fig. 9 Microscopy images of a 2 μm particle propagating down the Au–H_2O–Au waveguide.

dependent), which allows for particle separation by size along the device.

The measured propagation distance of 2 μm and 4 μm particles is experimentally shown in Fig. 10 and compared to the theoretical results. The results show a clear separation in position between the two particle sizes, and this positional distance is magnified during the propagation in the outer guide. The separation is larger than predicted by simulations and could be in part due to any errors in estimating the correct guided powers in the theoretical model to match experimental results.

To demonstrate the sorting abilities of our dual waveguides, a heterogeneous mixture of silicon dioxide beads was placed into the inlet port of the microfluidic system right above the dual-core waveguides. An input power of TM polarized light of 400 mW was coupled into the system to drive the particle movement and separation. As expected, each different particle size came to a stop at a different location along the outer guide. The final distances were measured from the entrance of the waveguide. The total distances travelled by each particle size and the stopping locations of the particles are shown in Fig. 11, which clearly demonstrates particle separation by size along the waveguide.

In addition, we conducted a repeatability test for coupling into the inner and outer waveguides and found that for $n = 4$ coupling trials, we obtained a guided power variation of ±1 mW for the inner guide and a guided power variation of ±0.5 mW for the outer waveguides. Variations in coupling effects introduce changes in the distances that particles travel and should be minimized for consistent testing conditions. The error bars in Fig. 11 give a sense of the variations in particle locations that may arise from coupling inconsistencies.

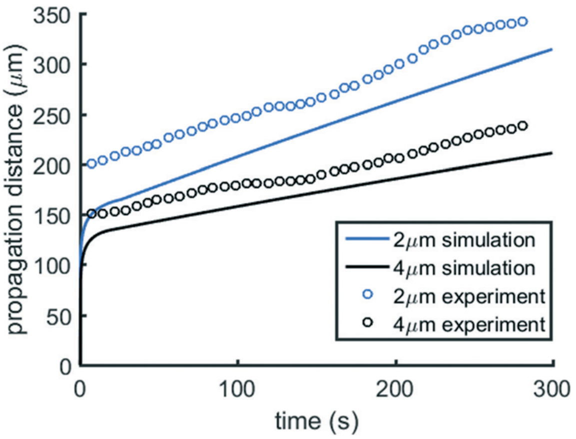

Fig. 10 Particle trajectory over time is plotted comparing the theory to the experimental results. The solid lines represent the simulated theoretical results and the empty circles represent the experimental results.

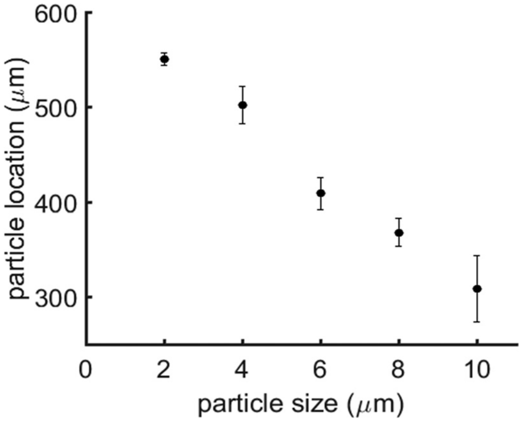

Fig. 11 The final distance travelled by 2–10 μm particles for an input power of 400 mW. This result shows the particle separation that occurs when the particles stop propagating along the waveguide. Error bars represent $n = 4$ for each particle size.

Conclusions

We have demonstrated a dual-core waveguide optical sorter that utilizes the intrinsic forces of MIM waveguides and their geometry to achieve high fidelity particle separation by size. The theory and simulations predict a size-dependent transition from the inner to the outer waveguide, and a size-dependent propagation length along the outer waveguide. Our fabricated waveguide sorters verified the predicted operation. The simplicity, robustness, and functionality of the optical system show that this sorting technology has the potential to become important for a number of applications in biology and chemistry where single-cell trapping and separation is desired.

Acknowledgements

SAK is supported by the Stanford Graduate Fellowship and the National Science Foundation Graduate Student Fellowship. The authors would like to thank Roger Howe, J Provine, and Michelle Rincon at the Stanford Nanofabrication Facilities for their advice and guidance on the sidewall metal deposition technique. We would also like to thank Yousif Kelaita, Nathan Loewke, Carsten Langrock, and Shanhui Fan for insightful conversations, as well as Tim Brand from the Ginzton Crystal Shop for help with optically polishing the waveguides.

References

1 A. Ashkin, *Methods Cell Biol.*, 1998, **55**, 1–27.
2 A. Ashkin, *Phys. Rev. Lett.*, 1970, **24**, 156–159.
3 J. R. Moffitt, Y. R. Chemla, S. B. Smith and C. Bustamante, *Annu. Rev. Biochem.*, 2008, **77**, 205–228.

4 L.-C. Hsu, T.-C. Chen, Y.-T. Yang, C.-Y. Huang, D.-W. Shen, Y.-T. Chen and M.-C. M. Lee, *Lab Chip*, 2013, **13**, 1151–1155.

5 H. Cai and A. W. Poon, *Lab Chip*, 2012, **12**, 3803–3809.

6 S. Gaugiran, S. Gétin, J. M. Fedeli, G. Colas, A. Fuchs and F. Chatelain, *Opt. Express*, 2005, **13**, 6956–6963.

7 Ø. I. Helle, B. S. Ahluwalia and O. G. Hellesø, *Opt. Express*, 2015, **23**, 6601.

8 A. H. J. Yang, T. Lerdsuchatawanich and D. Erickson, *Nano Lett.*, 2009, **9**, 1182–1188.

9 A. H. J. Yang, S. D. Moore, B. S. Schmidt, M. Klug, M. Lipson and D. Erickson, *Nature*, 2009, **457**, 71–75.

10 P. T. Lin, I. C. Lin, H. Y. Chu, T. W. Lu and P. T. Lee, *Int. Conf. Opt. MEMS Nanophotonics*, 2014, vol. 14, pp. 75–76.

11 A. H. Reshak, K. N. Khor, M. M. Shahimin and S. A. Z. Murad, *Prog. Biophys. Mol. Biol.*, 2013, **112**, 118–123.

12 P. Lovhaugen, B. S. Ahluwalia, T. R. Huser, P. McCourt and O. G. Helleso, *Proc. SPIE*, 2011, **7902**, 79020N.

13 B. S. Ahluwalia, P. McCourt, T. Huser and O. G. Hellesø, *Opt. Express*, 2010, **18**, 21053–21061.

14 K. Grujic, O. Hellesø, J. Hole and J. Wilkinson, *Opt. Express*, 2005, **13**, 1–7.

15 K. D. Leake, B. S. Phillips, T. D. Yuzvinsky, A. R. Hawkins and H. Schmidt, *Opt. Express*, 2013, **21**, 106–110.

16 S. Lin and K. B. Crozier, *Opt. Express*, 2012, **20**, 3367–3374.

17 S. A. Khan, Y. Shi, C.-M. Chang, C. Jan, S. Fan, A. K. Ellerbee and O. Solgaard, *Opt. Express*, 2015, **23**, 8855.

18 E. Cheng, H. Zou, Z. Yin, P. Jurčíček and X. Zhang, *J. Micromech. Microeng.*, 2013, **23**, 075022.

19 G. Zhu and N. Trung Nguyen, *Micro Nanosyst.*, 2010, **2**, 202–216.

20 R. Fuchs, T. Weinhart, J. Meyer, H. Zhuang, T. Staedler, X. Jiang and S. Luding, *Granular Matter*, 2014, **16**, 281–297.

21 L. P. Faucheux and A. J. Libchaber, *Phys. Rev. E: Stat. Phys., Plasmas, Fluids, Relat. Interdiscip. Top.*, 1994, **49**, 5158–5163.

22 J. S. Punjrath and D. R. Heldman, *J. Aerosol Sci.*, 1972, **3**, 429–440.

23 T. Cail and M. F. Hochella, *Environ. Sci. Technol.*, 2005, **39**, 1011–1017.

24 G. Veronis and S. Fan, *J. Lightwave Technol.*, 2007, **25**, 2511–2521.

25 W. Shin, 2015, https://github.com/wsshin/maxwellfdfd.

26 H. R. Philipp, *J. Electrochem. Soc.*, 1973, **120**, 295.

27 I. H. Malitson, *J. Opt. Soc. Am.*, 1965, **55**, 1205.

28 M. A. Green and M. J. Keevers, *Progr. Photovolt.: Res. Appl.*, 1995, **3**, 189–192.

29 A. D. Rakic, A. B. Djurisic, J. M. Elazar and M. L. Majewski, *Appl. Opt.*, 1998, **37**, 5271–5283.

30 G. M. Hale and M. R. Querry, *Appl. Opt.*, 1989, **12**, 555–563.

31 B. Chu, *Laser Light Scattering*, Academic Press, 1974.

32 P. Vettiger, *J. Vac. Sci. Technol., B: Microelectron. Process. Phenom.*, 1989, **7**, 1756.

33 H. Xin, H. Lei, Y. Zhang, X. Li and B. Li, *Opt. Express*, 2011, **19**, 2711–2719.

34 X. Miao, B. K. Wilson, L. Y. Lin, X. Miao, B. K. Wilson and L. Y. Lin, *Appl. Phys. Lett.*, 2008, **92**, 124108.